www.sciencemag.org/content/359/6380/1136/suppl/DC1

Supplementary Materials for

Ice-VII inclusions in diamonds: Evidence for aqueous fluid in Earth's deep mantle

O. Tschauner,* S. Huang, E. Greenberg, V. B. Prakapenka, C. Ma, G. R. Rossman, A. H. Shen, D. Zhang, M. Newville, A. Lanzirotti, K. Tait

*Corresponding author. Email: olivert@physics.unlv.edu

Published 9 March 2018, *Science* **359**, 1136 (2018)
DOI: 10.1126/science.aao3030

This PDF file includes:

Materials and Methods.

The type material of ice-VII, a roughly triangular fragment from a diamond macle (sample GRR1521, Table S1) with dimensions 350×420 μm^2 and 50-70 μm thickness is deposited in the collections of the Royal Ontario Museum, Toronto, Canada, with registration number M57666. An image of the specimen is shown in Fig. S1a. Weight and properties of the other specimens are given in Table S1.

Diffraction data were collected at the undulator beamline 13-IDD (GSECARS, APS, Argonne National Laboratory (34)) with hard X-rays (0.03344 nm) focused to 2×3 μm^2. Two patterns (Fig S4h and S5b) were collected at 16-IDB (HPCAT). A PILATUS 3X CdTe 1M pixel array detector was used for collecting diffraction data (PILATUS 1M at 16-IDB). Diffraction data were collected in forward scattering geometry with an acquisition time of 3 s per step, and for 10s per mapping increment for selected regions. Calibration was conducted with GSE-ADA (35) and DIOPTAS (36). Integration and correction for geometric distortion was conducted with DIOPTAS (36). X-ray micro-fluorescence maps were collected on beamline 13-IDE, GSECARS, APS, Chicago with a 2×3 μm^2 focused beam in 90º backscatter geometry using a Vortex detector. Rietveld refinement of the powder diffraction data (Fig. 1) showed the presence of preferred orientation along [211] in type ice-VII. The surrounding diamond matrix generates single crystal diffraction and diffuse elastic and inelastic scattering. A diffraction frame of pure diamond from nearby the ice inclusion was used for image background subtraction (whence, no diamond reflections appear in the integrated diffraction pattern in Fig. 1). For the type material we obtained for the Rietveld refinement an R_{wp} of 5.72% with an R_p of 4.57% with $\chi^2 = 1.71$ for 1398 observations. The LeBail-extraction converged to R_p =

4.0% using Powdercell (37). R_F was 4.0% (see Table S3), which shows that the assessment of the preferred orientation was correct and did not compromise the refinement of the structure. Other occurrences of ice-VII converge to R_{wp} between 3 and 7%. The pattern of type ice-VII contains a contribution from 0.7 – 0.8 vol. % of an adjacent inclusions of iron which had been refined along with ice-VII. Pseudovoigt peak profiles were used with Gaussian terms U = 0.489, V = 0.018, W = 0.08 and Lorentzian terms L_x = 0.344 and L_y = 0 (in Powdercell, ref. 37).

Presence of K and Cl was detected by micro-XRF mapping at beamline 13-IDE, APS. Na is not measurable because its X-ray fluorescence is absorbed by the host diamond crystal. Subsequently we constrain the amount of NaCl and KCl through Rietveld refinement of site occupancy. The phase contrast between O, Na, and K + Cl is quite pronounced and permits reliable convergence for data of present quality. Furthermore, the Na/K ratio is constraint by charge balance with Cl^-. We modelled Na and Cl occupancies for various sites in ice-VII. Earlier studies (26, 38) have indicated that Li-, K-, Na- and Cl-ions reside in ice-VII on the same site as oxygen and that no structural correlation occurs between dissolved ionic species (38). We confirm this observation for natural ice-VII (Table 1). Occupancies for any other site converged to zero.

Kuhs et al. (39) observed that oxygen in ice-VII at ambient pressure and low temperature does not strictly reside on site 2a but is better modelled by a partially occupied site 8e. We examined this O-sublattice disorder and find that it also occurs in natural ice-VII but the difference in refinement quality between O on site 8e and 2a is small with slight favour for 8e (Table S2).

In order to quantify absorption and to check possible extinction effects from the surrounding diamond single crystal host, we conducted a LeBail extraction and compared calculated and observed |F(hkl)|. No extinction and only insignificant absorption was found (see Table S1, we note that the diamond host crystal M57666 is only 50-80 micrometer thick). We conducted a reversed Monte Carlo (rMC) optimization (40) without bias by atomic potentials and Rietveld refinement to check possible constraints on the proton position. rMC has been found to be useful for assignment of proton positions from X-ray diffraction data even those obtained in high pressure diamond cells (41). The resulting proton position from rMC agrees with the result of the Rietveld refinement within 5% but we note that the profile-weighted R_{wp} for modelled pattern with and without protons differs by only 2.6% (R_{wp} = 5.72 versus 5.87%). Thus, the contribution of protons to the observed pattern is marginally significant (as expected). Our finding of protons residing on site 8e is consistent with high pressure neutron diffraction studies on D_2O at ~ 10 GPa (42). Figure S3 shows observed and modelled refined pattern of ice-VII from all examined specimens.

(Na,K)Cl·$5H_2O$ is a clathrate similar to ice-VII but with volume expanded to 88.1 $Å^3$ (43) and part of the alkali-halide residing on site 6d.

Characterization by infrared spectroscopy

IR-spectra were obtained in transmission mode with a Thermo-Nicolet iS50 spectrometer at the Division of Geology and Planetary Sciences at Caltech with 2 cm^{-1} resolution at room temperature (23°C), with a CaF_2 beam splitter, a quartz-halogen tungsten source, and an HgCdTe LN_2-cooled detector, and at ALS bending magnet beamline 1.4.with a

Nicolet Magna 760 FTIR bench and a Nic-Plan IR microscope with 32× magnification Schwarzschild objective, with 1 cm^{-1} resolution and a HgCdTe detector with a KBr beam splitter. Figure S3 shows spectra over the rage from 600 to 4000 cm^{-1} (Fig. S2a), O-H bending- and symmetric stretching bands in background subtracted spectra (Fig. S2b), and the combination band (Fig. S2c). In addition, absorption bands of free water around 3400 cm^{-1} are visible in the spectra of specimens GRR1521 and 1507 (Fig. S2a). These spectra also show carbonate absorption bands around 1640 cm^{-1} and bear typical spectral features of fibrous diamonds. Both diamonds have rims of fibrous diamond around clear kernels whereas SM458 has a clear rim around an inclusion-rich kernel (Fig. S1b). With the spatial resolution of our IR spectral analysis these different regions in the specimens could not be well separated. Our X-ray fluorescence maps show the transition between rim and kernel clearly while inclusions of carbonate, halide, and ice occur separately in the kernels of the specimens (Fig. S1b). The fluorescence maps were used to define regions of interest in the X-ray diffraction maps. All of our specimens exhibit low levels of nitrogen-aggregation, compared to known ultra-deep diamonds (16). This suggests that our samples are rather young (implying very fast ascent) or have remained at temperatures that are low compared to the average TZ. We suggest that this apparent low nitrogen-aggregation is a consequence of the heterogeneity of the host diamonds rather than unusually fast ascent or temperature. We observe mosaicity of the diamond lattices through X-ray diffraction and we see zoning and domains through XRF mappings (Fig. S1b). We suggest that the IR transmission spectra average over younger zones and elder kernels of the same diamond specimen whereas the X-ray probe samples these domains with much higher spatial resolution than IR-spectroscopy. Some domains of the

diamonds can be much older than others. One may argue that the diamonds should have equilibrated in the mantle, but this assumes the whole diamond specimen has grown in greater depth. If elder kernels are merged through continued diamond growth in the lithosphere, there is no discrepancy.

Estimation of the current inclusion pressures

Current residual pressures were determined through a third order Birch-Murnaghan equations of state of ice-VII. We use V_0, B_0, and B_0' of pure ice-VII from Frank et al. (26). The effect of dissolved ionic species such as NaCl, KCl, and LiCl on the volume of ice-VII has been studied but different groups come to contrary conclusions whether alkali halides induce positive (27, 37, 43) or negative (26) excess volume. Therefore, we calculate current residual pressure based on the equation of state of pure ice-VII and use the difference to the equation of state of ice-VII with 1.8 mol% NaCl (26) to define uncertainty. Thereby, a possible positive or negative excess volume is accounted for as uncertainty of pressure. Pressure estimate for GRR1518 is based on the volume of NaCl (46) but without assessing the excess volume of the minor KCl component. Thus, pressure is a lower estimate.

Pressures of inclusions of ilmenite, halite, and magnesian calcite were determined based on experimentally established equations of state (46, 47, 48. 49). Tronche et al. (47) have examined a natural ilmenite-geikielite solid solution with composition similar to present one (Table 1) and their equation of state was directly used in our computation. Magnesian calcite of the present composition has not been examined but it has been

established that the product of bulk modulus and volume of Ca- and Mg-carbonates in the calcite- and dolomite-series are constant within uncertainties (48, 49). Thus, we used the mixing volume at ambient pressure (50) as reference volume and the interpolated bulk modulus and it's pressure derivative of the solid solution (49) to determine the pressure of magnesian calcite. We used an ambient pressure volume of 246 $Å^3$, K = 85 GPa and K_0' of 3 (49)

Estimation of entrapment pressures

We explored two independent methods for constraining the pressure of entrapment of ice-VII in diamond. One method is based on the low compressibility and thermal expansion of diamond and assumes that the current residual pressure of the inclusion and the pressure and temperature of its entrapment are connected through a path that is close to an isochore (19, 20).The other method is based on isomekes (33). Ultimately the accuracy of the results from both methods are limited by the rather large uncertainties of the thermoelastic properties and equations of state of diamond, ice-VII, and, particularly, of fluid dense H_2O.

We discuss the isochoric approach first. We note that diamond is not strictly incompressible over the relevant pressure-temperature range although compressibility and thermal expansion partially compensate each other. We use a Murnaghan-type equation of state for diamond because the compression of diamond over the relevant pressure range is nearly linear (51, 52) while error propagation is reduced by using this simpler equation of state rather than the more complex functionals of the Birch-Murnaghan- or Vinet-type. The bulk modulus of diamond ranges from 430 to 447 GPa

(51-53). We use the experimentally assessed linear temperature dependence of thermal expansion of diamond that had been measured between 500 – 900 K (54) in order to determine the thermoelastic contribution to the equation of state. Since the pressure derivative of the thermal expansivity of diamond is poorly known and since we are interested in a pressure interval where this pressure-dependence is negligible we assume thermal expansivity to be pressure-independent over the examined range of densities. We find that at 15 GPa, 1700 K a volume expansion of diamond of 0.6 – 1.0% and at 25 GPa, 2000 K 0.8-1.2%. We add these excess volumes to the volume of ice-VII and fluid H_2O at given pressures and temperatures and calculate the effective pressure-reduction that results from the excess volume. For instance for 15 GPa, 1700 K and 25 GPa, 2000 K, we find pressure reductions of 0.5 – 0.8 and 0.8 – 1.2 GPa, respectively. As we will show, markedly larger uncertainties arise from the equations of state themselves (see also Fig. 2). Therefore, we consider the deviation from the isochoric path for the relevant pressure-temperature range and for fluid or solid ice inclusions in diamond as negligible within given uncertainties. We note that this approximation is acceptable for comparatively soft inclusions in diamond but it fails for softer host minerals.

In a next step we determine the pressures of the inclusions after correction for the local deformation of diamond around the inclusions (33). In principle we can constrain this local deformation of host diamond because our diffraction data were collected with a micro-focused beam in mapping mode. Hence, the difference between the diffraction signal of diamond reflections at the locations of the inclusions and 40-60 μm afar gives an estimate of local deformation of diamond around the inclusion relative to the unstrained lattice. That, in turn, allows for determining the average stress (pressure) of

diamond surrounding the inclusion within the 3-4 μm radius of the beam focus. However, the host diamond lattice is not entirely unstrained in most of our samples and in fact, varies over inclusion-free regions of several ten to a few hundred μm in length. Thus, we can only give a maximal local host stress of ~0.3 GPa. Because of this uncertainty it is also futile to attempt a more sophisticated modelling of the local stress field.

After correction of residual pressures for elastic relaxation (Table 1) we determine entrapment pressures as the intersection points of isochores of ice-VII and fluid H_2O with the three adiabates that are shown in Fig. 2b, similar to the approach in references (19,20). Right away it is clear that these pressure-temperature paths have rather steep slopes $\Delta T/\Delta P$ and that any possible intersection occurs within the stability field of fluid H_2O rather than ice-VII (Fig. 2). The melting curve of ice-VII remains a matter of active debate (55-57). In Fig. 2 we bracket the range of published data using the melting curves reported in references 56 and 57. We do not further consider the isochores of ice-VII and focus on the isochores of fluid H_2O. The steep overall $\Delta T/\Delta P$ is result of changes in slope of the isochores over the relevant pressure-temperature range (see below).

Two experimental studies have examined the density of fluid H_2O in the pressure-temperature range of 1-7 GPa and 100-700 K (58, 59). In addition there are shock-compression studies at substantially higher pressures and temperatures whose results we do not use here directly, which, however, are implemented in the equation of state of fluid H_2O by Abrahmson and Brown (58). We calculate isochores of H_2O based on both studies (58, 59) and use their discrepancies as measure of 1-σ uncertainty and the 1-σ uncertainties given in (56). The resulting range of pressure-temperature paths is shown as hashured regions in Fig.2. The same procedure was applied to an inclusion of ilmenite in

specimen GRR1507 (Table 1, Fig. S4a) using the equation of state for natural ilmenite of similar composition (47). The results give entrapment conditions in the same pressure-temperature interval as ice-VII from the same host diamond GRR1507 (Fig. 2).

We ignore the possible effect of dissolved alkali halides on the equation of state of fluid H_2O because it is unknown. For some of the observed inclusions of ice-VII this effect can be assumed to be small because the amount of alkali halide is small (Table 1).

We note that the isochores based on (59) exhibit noticeable curvature in the 10-30 GPa regime. This non-linear slope can be artifactual and result of the extrapolation of the equation of state quite beyond its experimental basis. However, we note that the isochores from both independent studies (58, 59) agree within uncertainties. This curvature is the main reason for the overall small thermal pressure effect that related current residual to entrapment pressure.

Angel et al. (33) have presented a more general approach for obtaining entrapment conditions from equations of state and residual pressures of inclusions and hosts. This approach is based on isomekes (33). We use the method outlined by Angel et al. (33) to obtain residual pressures corrected for elastic relaxation (see above and Table 1) and for constructing isomekes. For a residual pressure of 11 GPa, corrected for relaxation, we obtain P_{foot} (33) of 12 GPa for a pressure of 23 GPa we obtain P_{foot} of 24 GPa. By error propagation these pressures have uncertainties of 1.2 and 3 GPa, respectively. The incremental slope of the isomeke is given by the difference of thermal expansivity over the difference of the compressibility of the inclusions and their host phases (33). Since ice-VII and fluid H_2O are about 20-times more compressible than diamond and since ice-VII and fluid H_2O have more than ten times higher thermal

expansivity than diamond the isomeke is within good approximation an isochore of ice-VII or fluid H_2O, respectively, and the isomekes are within the hachured regions in Fig.2b. The isomekes will provide more accurate estimations than the isochoric approximation once significantly more accurate thermoelastic properties of the involved phases become available.

Encapsulation of fluid

Water-bearing saline (22, 23) or carbonaceous (19) inclusions in diamonds have been described earlier. The aqueous inclusions described in these studies were found to be very silicate-rich, rather being hydrous saline melts than fluids (22). They occur in the fibrous rims of diamonds. In our study ice-VII as well as other fluid-derived inclusions like halite and carbonates were found in separate inclusions rather than as phase assemblies (Table 1, Fig. S1b). A possible explanation is based on the dimensions of these inclusions: On the small spatial scale of the inclusions encapsulation of multiple phases in single cavities is not favourable because of the relatively high contribution of interfacial energy to the free energy of such small phase assemblies. This may be different for the larger fluid inclusions observed in fibrous diamonds in earlier studies (21,22).

We note that specimens GRR1507, 1518, and 1521 are diamonds with fibrous rims around optically clear kernels. SM458 has a clear rim around an inclusion-rich kernel (Fig. S1b), and Balas is a polycrystalline diamond with inclusions throughout, but an outer zone much richer in inclusions than the interior. The different zones in our specimens are not well separated by IR-spectroscopy (Fig S2). However, X-ray fluorescence maps clearly show the rim-kernel boundaries through differences in trace-

element concentrations in the diamond matrix (Fig S1b). We note that fluid-derived inclusions like carbonates and halides occur in both the rims and the kernels of the specimens (Fig. S1b). Ice-VII and other high-pressure inclusions (Table 1, Fig. S3 and S4) are found in the kernels. They are rather fine grained polycrystalline whereas inclusions in the rims are much coarser with crystallite sizes > ½ μm to several μm, giving arrays of diffraction spots rather than Debye fringes. In GRR1518 we examined the fibrous rim of the diamond and found hydrous halite instead of ice-VII at a pressure typical for inclusions in fibrous rims (Table 1, 21).

Table S1: General properties of the ice-VII hosting diamonds.

Specimen	Type	Colour	Habit, appearance	Weight
GRR1518	IaAB	Green, no fluorescence	Cubic, hexagonal pits and channels	31.1*, cut and polished piece
GRR1507	IaAB, platelets prominent	Green rim rich in inclusions1, clear kernel, no fluorescence	Octahedron, faces frost and with trigons	85.6*, piece cut polished ‖ (001)
GRR1521	IaAB	Green, no fluorescence	Macle with many trigons and some pits	49.8, crushed, some pieces clear, some green
M57666	IaAB	Clear	Clear fragment from GRR1521	<1mg
SM458	IaAB	Clear, cloudy kernel	Octahedron	5mg, cut and polished
Balas	IaAB, platelets pronounced	Translucent. Polycrystalline rim, kernel with cloudy regions	Polycrystals are trisoctahedral, spherical shape	1g*, small piece mechanically removed (lost)

*Original weight in mg

Table S2: Fractional atom coordinates, site fraction occupancies, and isotropic thermal displacement factors of ice-VII and 1-σ uncertainties in brackets.

Atomic coordinates and isotropic displacement parameters (in Å^2)

Atom	**SFO**	**Wyck.**	**x**	**y**	**z**	**B_{iso}**
O	0.241(2)	8e	0.011(7)	0.011(7)	0.011(7)	0.13(6)
Na+Cl[a]	0.014(2)	8e	0.011(7)	0.011(7)	0.011(7)	0.13(6)
K+Cl[a]	0.008(2)	8e	0.011(7)	0.011(7)	0.011(7)	0.13(6)
H	0.482[b]	8*e*	0.32(2)	0.32(2)	0.32(2)	0.13[c]

[a]Na, K, and Cl all reside on the same Wyckoff site (in agreement with ref.s 26, 38). Thus, we cannot discriminate NaCl from KCl via diffraction-based analysis and the relative proportion of both species is strictly correlated: Therefore, we only give the upper limits for both species noting that the amounts of KCl and NaCl are correlated as $(11+17)/(19+17)\cdot X_{KCl} = X_{NaCl}$.
[b]Fixed, based on refined O-occupancy.
[c]Fixed

Table S3. List of observed and calculated factor moduli of ice VII (M = multiplicity).

h	**k**	**l**	**M**	**d(Å)**	**$\|F_{calc}\|$**	**$\|F_{obs}\|$**	**$\Delta\|F\|$**
1	1	0	12	2.237	1000.5	1000.0	0.5
1	1	1	8	1.826	80.8	76.9	3.9
2	0	0	6	1.582	686.1	709.4	-23.3
2	1	1	24	1.291	615.4	581.2	34.2
2	2	0	12	1.118	560.3	564.1	-3.8
2	2	1	24	1.054	12.6	17.1	-4.5
3	1	0	24	1.000	456.7	495.7	-39.0
3	1	1	24	0.954	15.3	17.1	-1.8
2	2	2	8	0.913	399.8	350.4	49.4
3	2	1	48	0.845	369.1	384.6	-15.5
4	0	0	6	0.791	324.9	324.8	0.1

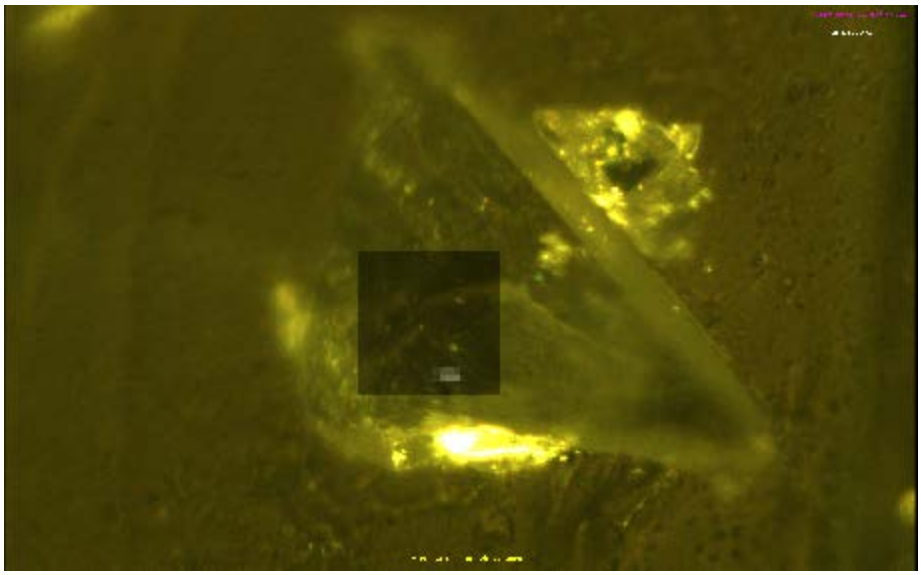

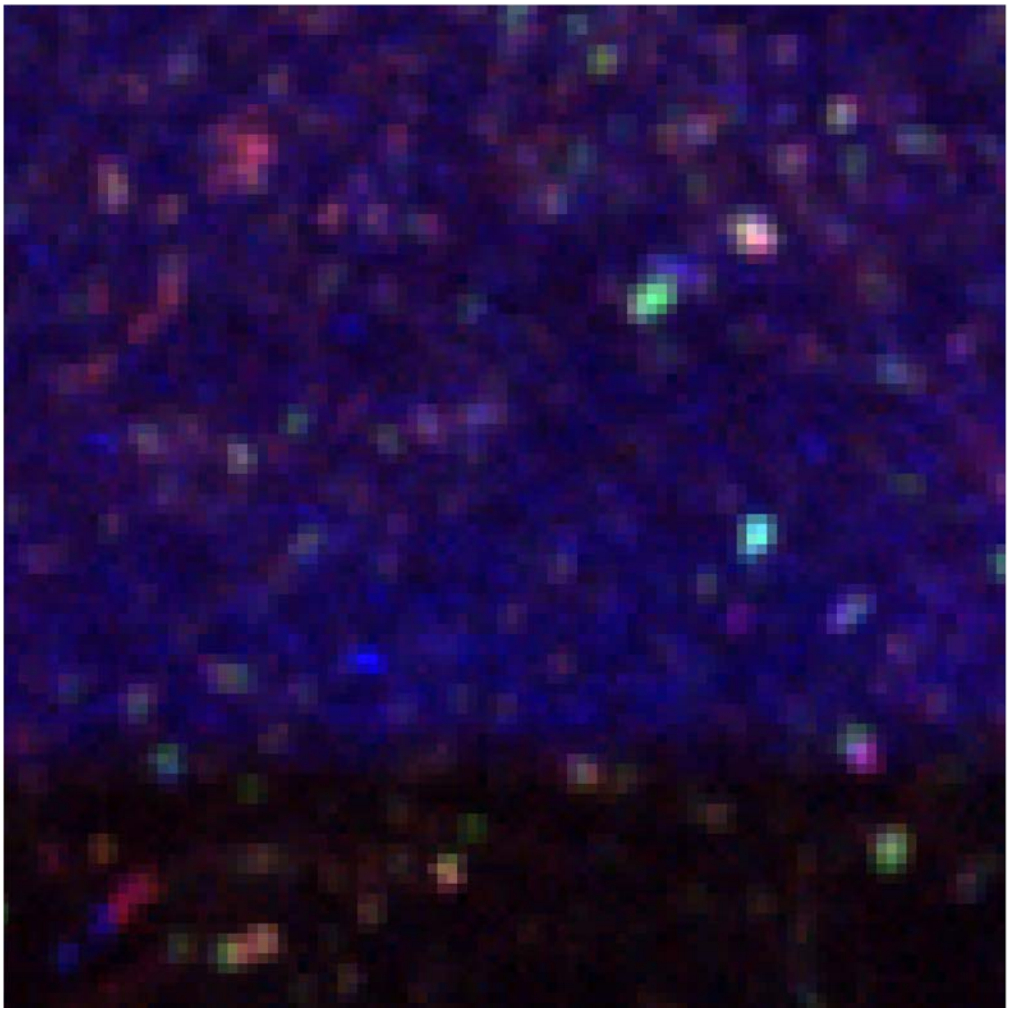

Fig. S1. Visible light and X-ray fluorescence images of samples. a: Visible light microscope image of the holotype ice-VII bearing diamond sample M57666 (a fragment of GRR1521, Table S1) mounted at the

diffractometer at beamline 13IDD, APS. The inclusions are not resolved by light microscopy. A diffraction imaging map of ice-VII type material is superimposed on the microscope image: The integrated area of the 111 diffraction peak was used as measure of abundance of ice-VII (*36*). Each pixel corresponds to one diffraction frame collected over a 5×5 μm^2 grid. Various smaller inclusions of ice-VII were observed in the holotype specimen. Since attenuation over the thickness of the diamond host crystal is negligible, the intensity distribution corresponds directly to the volume of ice-VII per pixel. In the present case it suggests a wedge-like, sphenoidal (that is: with hexakisoctahedral faces) or tilted trigon-like shape of the inclusion as it is also found as pitchmarks on diamond faces, for instance, at the original surface of the original diamond crystal GRR1521 (see Table S1).

b: X-ray fluorescence map of a region in specimen SM458 (Table1). The map is RGB-color coded for K, Ca, and Ti. Each pixel is defined by the X-ray beamsize of 2×4 μm^2. An equivalent map was obtained for Cl, Ca, Ti. The border between the outer rim and the kernel of the diamond is visible by a marked change in Ti-trace concentration in the diamond matrix. K (and Cl) mark halite inclusions, Ca marks carbonate and silicate inclusions. The inclusions are examined by X-ray diffraction. We note that halite and carbonate inclusions occur not only in the rim but also in the kernel of the diamond (and partially appear to intersect the rim because of the octahedral shape of the kernel). Ice-VII is not visible in the fluorescence map but occurs also in the kernel of the specimen. The ice-VII holotype sample M57666 is a small fragment from the kernel of a diamond with fibrous rim (Table S1). Same as the kernel of SM458 it shows an elevated Ti-concentration.

Fig S2a

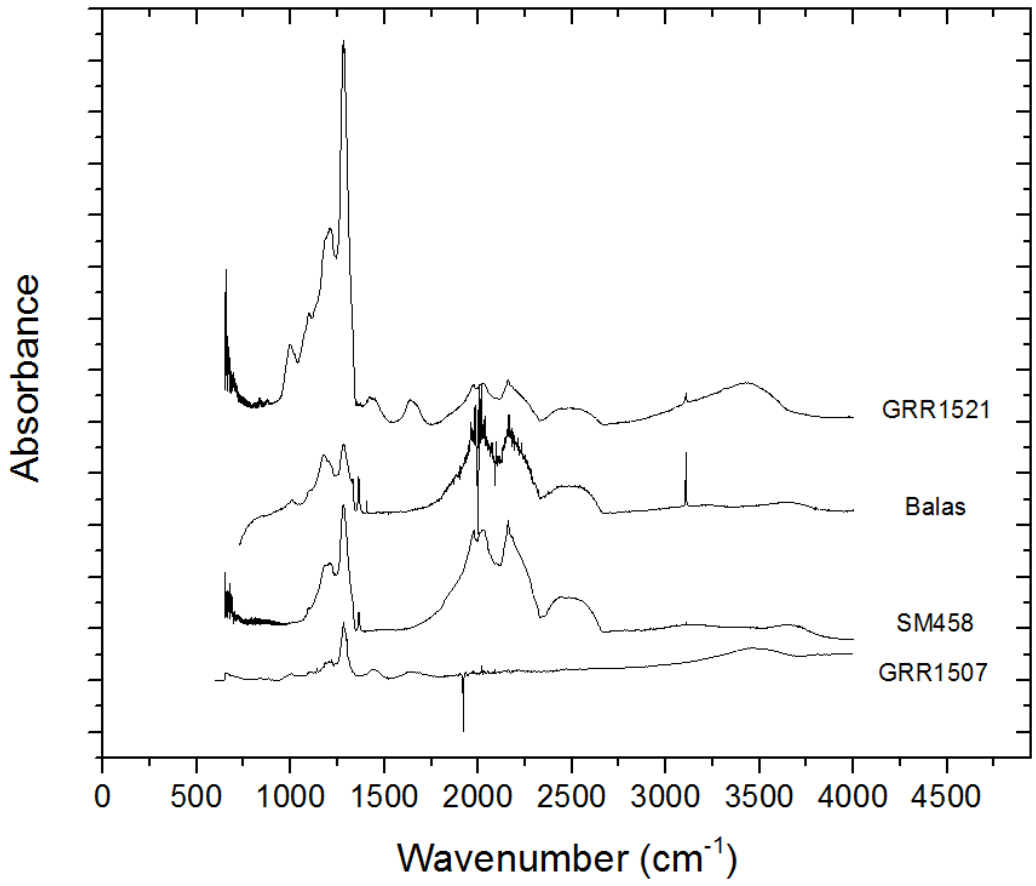
Absorbance
GRR1521
Balas
SM458
GRR1507
0
500
1000
1500
2000
2500
3000
3500
4000
4500
Wavenumber (cm-1)

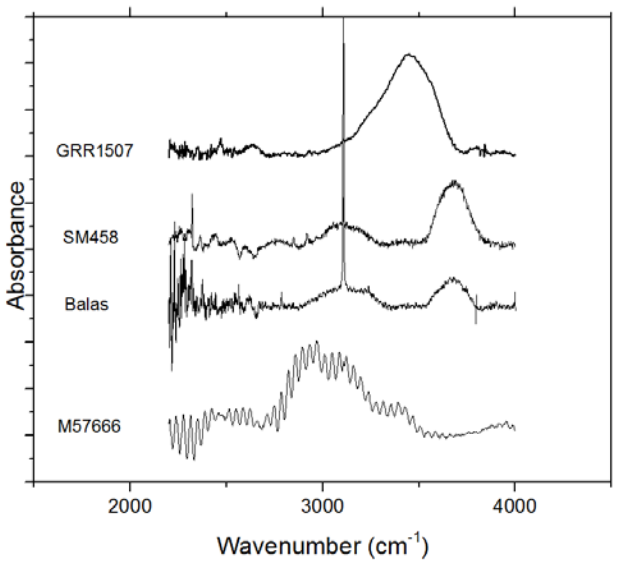

b.

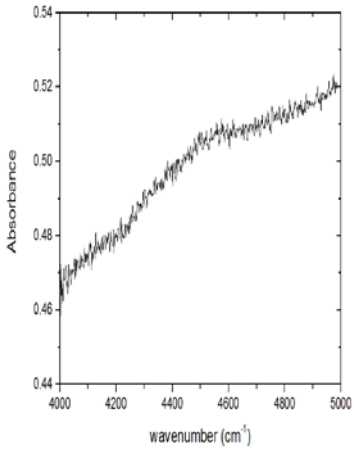

c.

Fig. S2: IR transmission spectra of ice-VII bearing diamonds. a) Full spectral range. The host diamonds exhibit A-, B-, and D-type defects.. b) The observed ice-related absorption bands are located between 3000 -3200 cm^{-1} with shoulder at slightly higher energy are from the ν_1 and ν_3 symmetric OH-stretching modes in ice VII (44,45). Based on the experimentally determined pressure dependence of these modes (44,45) the energy of these modes corresponds to pressures above 5 and below 23 GPa pressure. The spectrum from GRR1521 in (a) was obtained from a larger and thicker piece of GRR1521 than the type materials M57666 (GRR1521 had been crushed in an earlier analytical study many decades ago and M57666 is one piece of it, see Table S1). C.) Combination band of ice-VII in Balas-1. The combination band has been proposed to be a better indicator of residual pressure of ice-phases in diamond than the O-H stretching bands (24) but is quite weak. Extrapolating the correlation reported in (24) from ≤ 8 GPa we obtain an approximate pressure of 18±4 GPa for this sample (24 ±2 GPa from diffraction).

Fig. S3a

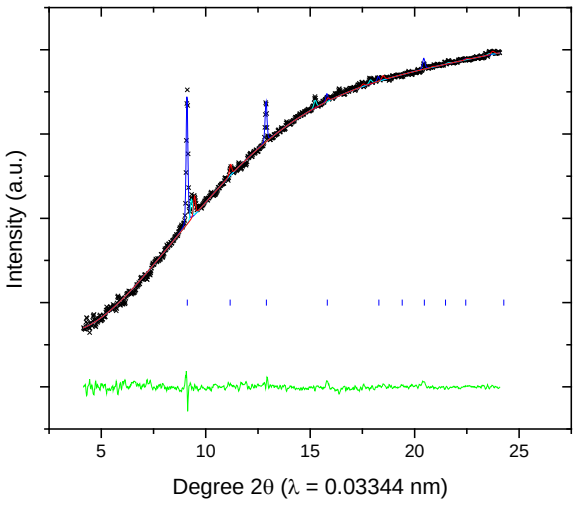

Fig. S3b

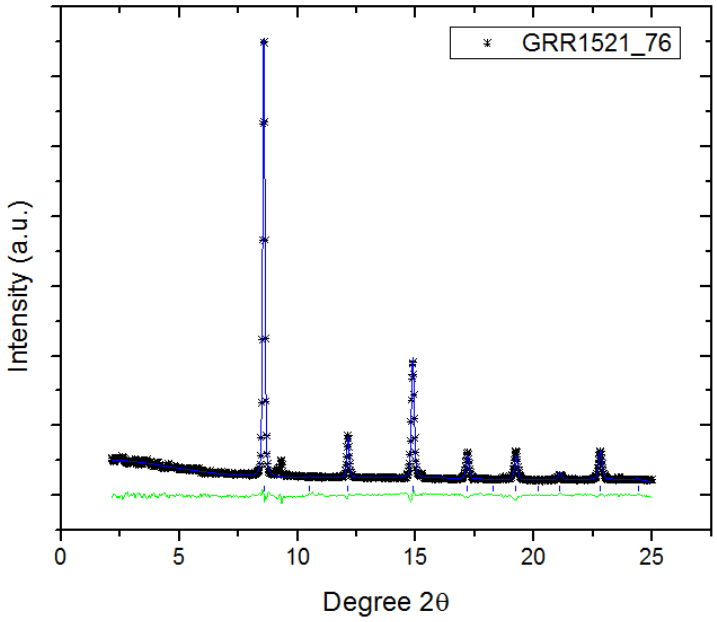

Fig. S3c

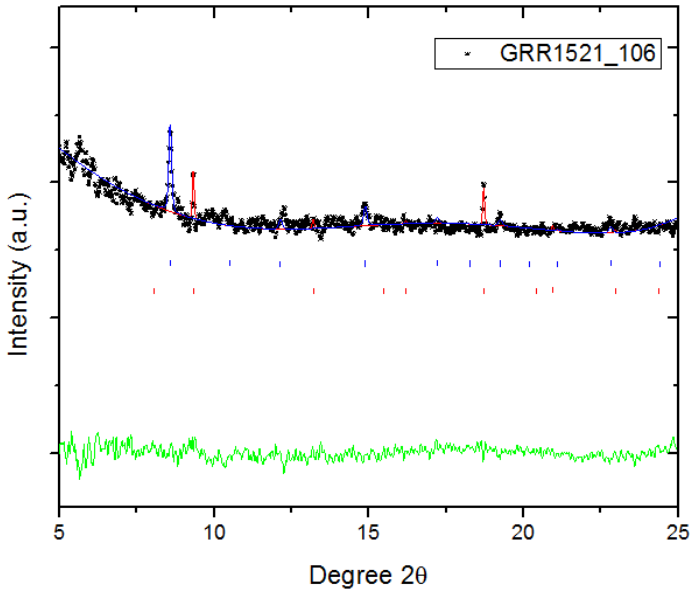

Fig. S3d

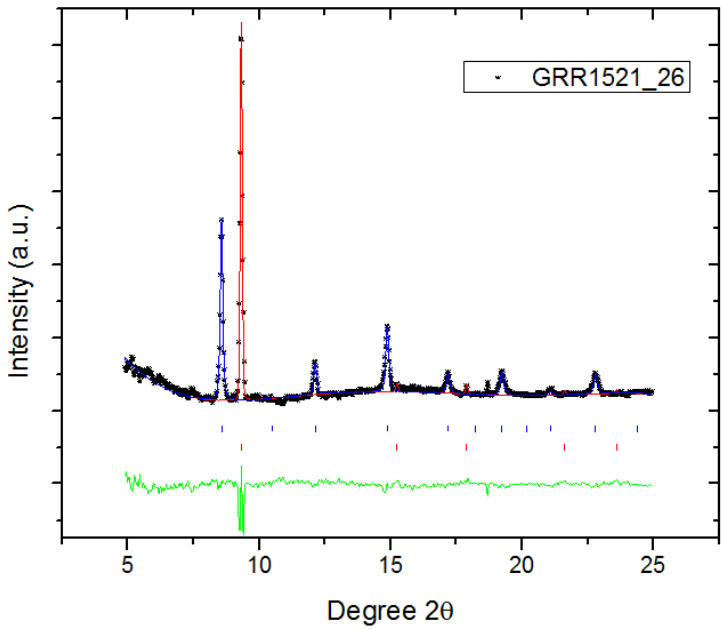

Fig. S3e

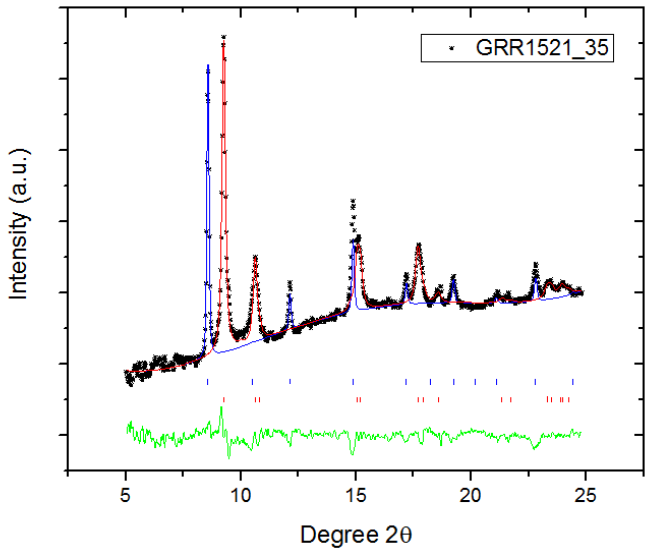

Fig. S3f

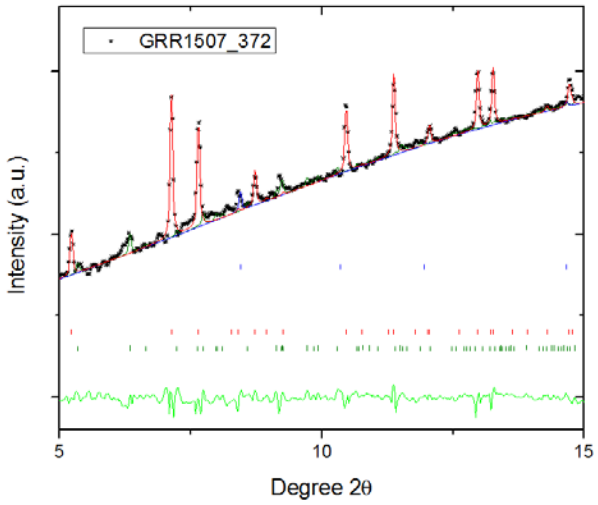

Fig. S3g

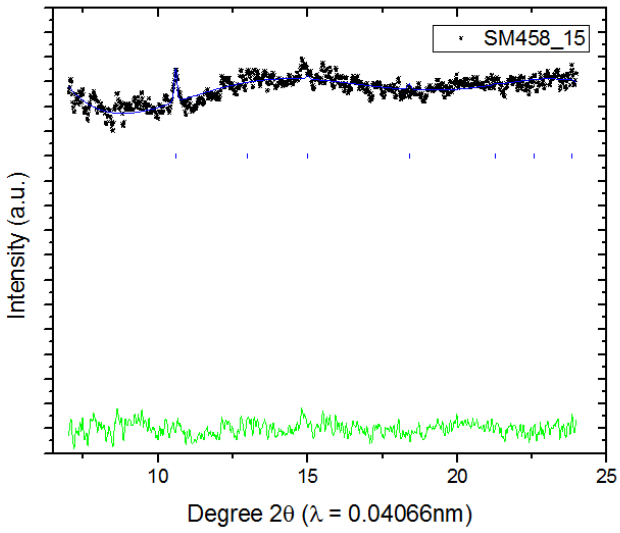

Fig. S3h

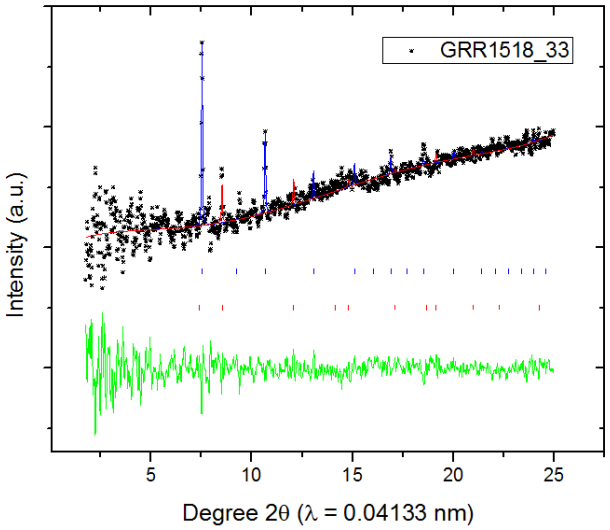

Fig. S3: Observed and modeled refined powder diffraction pattern of ice-VII. Black crosses = observed pattern, blue line: modeled, refined pattern of ice-VII, bright green: residuum of fit, other colors: other phases observed in the pattern a: diamond, (Fe,Ni,C), b: (Fe,Ni,C), c: diamond, d: diamond, e: (Fe,Ni,C), f: ilmenite, calcite, h: halite-sylvite. (Fe,Ni,C) assumes a tetragonally distorted bcc-structure. For each host specimen one pattern is shown. We also show additional patterns of ice-VII from the holotype diamond. Most patterns were obtained at wavelength 0.03344 nm, if different, wavelength is indicated in the abscissa.

Fig. S4a

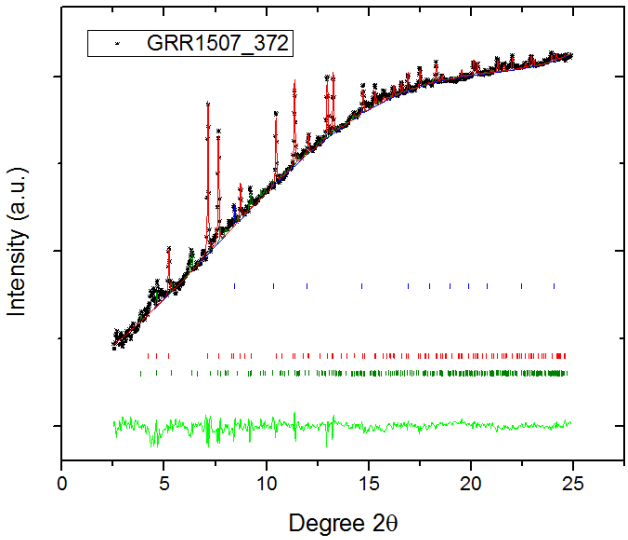

Fig. S4b

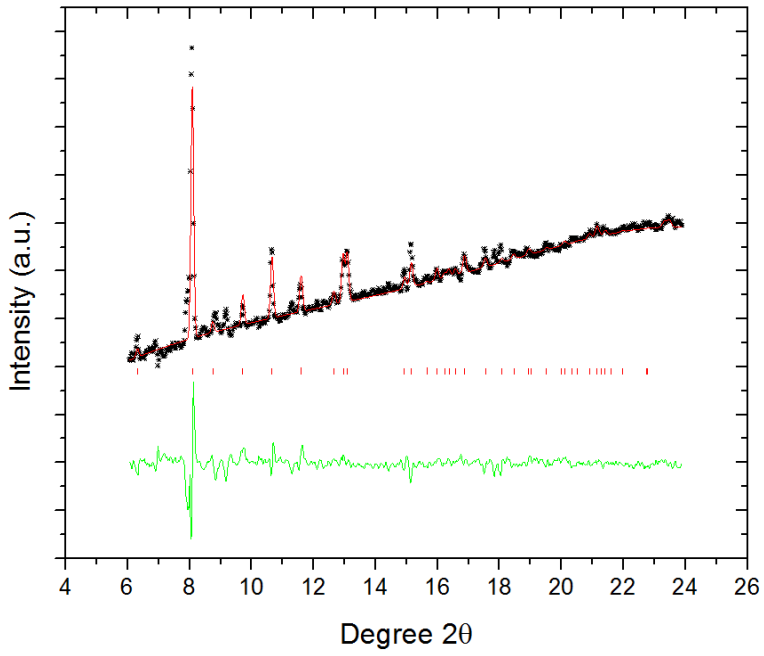

Fig. S4: Diffraction patterns of other inclusions which reside at high residual pressures: a) Ilmenite plus ice-VII in GRR1507 (see Fig. 2 and Table 1). Black crosses = observed pattern, red line: modeled pattern of ilmenite, blue line: modeled pattern of ice-VII, bright green: residuum of fit. b) magnesian calcite in SM458 (see Table 1). Black crosses = observed pattern, red line: modeled, refined pattern, bright green: residuum of fit. The volume and composition of magnesian calcite correspond to 8-9 GPa pressure. Composition and volume of ilmenite correspond to 11-12 GPa.

References

1. S. Karato, Water in the evolution of the Earth and other terrestrial planets. In *Treatise on Geophysics*, G. Schubert, Ed. (Elsevier, 2015), pp. 105–144.

2. T. L. Grove, C. B. Till, E. Lev, N. Chatterjee, E. Médard, Kinematic variables and water transport control the formation and location of arc volcanoes. *Nature* **459**, 694–697 (2009). doi:10.1038/nature08044 Medline

3. S. G. Nielsen, H. R. Marschall, Geochemical evidence for mélange melting in global arcs. *Sci. Adv.* **3**, e1602402 (2017). doi:10.1126/sciadv.1602402 Medline

4. H. Jung, Karato S, Water-induced fabric transitions in olivine. *Science* **293**, 1460–1463 (2001). doi:10.1126/science.1062235 Medline

5. N. Métrich, V. Zanon, L. Créon, A. Hildenbrand, M. Moreira, F. O. Marques, Is the 'Azores hotspot' a wetspot? Insights from the geochemistry of fluid and melt inclusions in olivine of Pico basalts. *J. Petrol.* **55**, 377–393 (2014). doi:10.1093/petrology/egt071

6. L. H. Rupke, J. P. Morgan, M. Hort, J. A. D. Connolly, Serpentine and the subduction zone water cycle. *Earth Planet. Sci. Lett.* **223**, 17–34 (2004). doi:10.1016/j.epsl.2004.04.018

7. D. R. Bell, G. R. Rossman, Water in Earth's mantle: The role of nominally anhydrous minerals. *Science* **255**, 1391–1397 (1992). doi:10.1126/science.255.5050.1391 Medline

8. S. Karato, Water distribution across the mantle transition zone and its implications for global material circulation. *Earth Planet. Sci. Lett.* **301**, 413–423 (2011). doi:10.1016/j.epsl.2010.11.038

9. T. Inoue, T. Wada, R. Sasaki, H. Yurimoto, Water partitioning in the Earth's mantle. *Phys. Earth Planet. Inter.* **183**, 245–251 (2010). doi:10.1016/j.pepi.2010.08.003

10. B. Schmandt, S. D. Jacobsen, T. W. Becker, Z. Liu, K. G. Dueker, Dehydration melting at the top of the lower mantle. *Science* **344**, 1265–1268 (2014). doi:10.1126/science.1253358 Medline

11. D. Bercovici, S. Karato, Whole-mantle convection and the transition-zone water filter. *Nature* **425**, 39–44 (2003). doi:10.1038/nature01918 Medline

12. F. E. Brenker, T. Stachel, J. W. Harris, Exhumation of lower mantle inclusions in diamond: ATEM investigation of retrograde phase transitions, reactions and exsolution. *Earth Planet. Sci. Lett.* **198**, 1–9 (2002). doi:10.1016/S0012-821X(02)00514-9

13. T. Stachel, J. W. Harris, G. P. Brey, W. Joswig, Kankan diamonds (Guinea) II: Lower mantle inclusion parageneses. *Contrib. Mineral. Petrol.* **140**, 16–27 (2000). doi:10.1007/s004100000174

14. D. G. Pearson, F. E. Brenker, F. Nestola, J. McNeill, L. Nasdala, M. T. Hutchison, S. Matveev, K. Mather, G. Silversmit, S. Schmitz, B. Vekemans, L. Vincze, Hydrous

mantle transition zone indicated by ringwoodite included within diamond. *Nature* **507**, 221–224 (2014). doi:10.1038/nature13080 Medline

15. N. V. Sobolev, F. V. Kaminsky, W. L. Griffin, E. S. Yefimova, T. T. Win, C. G. Ryan, A. I. Botkunov, Mineral inclusions in diamonds from the Sputnik kimberlite pipe, Yakutia. *Lithos* **39**, 135–157 (1997). doi:10.1016/S0024-4937(96)00022-9

16. S. B. Shirey, P. Cartigny, D. J. Frost, S. Keshav, F. Nestola, P. Nimis, D. G. Pearson, N. V. Sobolev, M. J. Walter, Diamonds and the geology of mantle carbon. *Rev. Mineral. Geochem.* **75**, 355–421 (2013). doi:10.2138/rmg.2013.75.12

17. O. Tschauner, E. Greenberg, V. Prakapenka, C. Ma, K. Tait, Ice-VII, IMA 2017-029. CNMNC Newsletter No. 38, August 2017, page 1036. *Mineral. Mag.* **81**, 1033–1038 (2017).

18. V. F. Petrenko, R. W. Whitworth, *Physics of Ice* (Oxford Univ. Press, 1999), p. 253.

19. O. Navon, High internal pressures in diamond fluid inclusions determined by infrared absorption. *Nature* **353**, 746–748 (1991). doi:10.1038/353746a0

20. O. Navon, R. Wirth, C. Schmidt, B. M. Jablon, A. Schreiber, E. Emmanuel, Solid molecular nitrogen (δ-N_2) inclusions in Juina diamonds: Exsolution at the base of the transition zone. *Earth Planet. Sci. Lett.* **464**, 237–247 (2017). doi:10.1016/j.epsl.2017.01.035

21. E. S. Izraeli, J. W. Harris, O. Navon, Brine inclusions in diamonds: A new upper mantle fluid. *Earth Planet. Sci. Lett.* **187**, 323–332 (2001). doi:10.1016/S0012-821X(01)00291-6

22. Y. Weiss, I. Kiflawi, O. Navon, The IR absorption spectrum of water in microinclusion-bearing diamonds. In *Proceedings of 10th International Kimberlite Conference* (Springer, 2013), pp. 271–280.

23. H. Kagi, R. Lu, P. Davidson, A. F. Goncharov, H. K. Mao, R. J. Hemley, Evidence for ice VI as an inclusion in cuboid diamonds from high P-T near infrared spectroscopy. *Mineral. Mag.* **64**, 1089–1097 (2000). doi:10.1180/002646100549904

24. E. M. Smith, S. B. Shirey, F. Nestola, E. S. Bullock, J. Wang, S. H. Richardson, W. Wang, Large gem diamonds from metallic liquid in Earth's deep mantle. *Science* **354**, 1403–1405 (2016). doi:10.1126/science.aal1303 Medline

25. J. M. Brown, T. J. Shankland, Thermodynamic parameters in the Earth as determined from seismic profiles. *Geophys. J. R. Astron. Soc.* **66**, 579–596 (1981). doi:10.1111/j.1365-246X.1981.tb04891.x

26. See supplementary materials.

27. M. R. Frank, E. Aarestad, H. P. Scott, V. B. Prakapenka, A comparison of ice-VII formed in the H_2O, NaCl-H_2O, and CH_3OH-H_2O systems: Implications for H_2O-rich planets. *Phys. Earth Planet. Inter.* **215**, 12–20 (2013). doi:10.1016/j.pepi.2012.10.010

28. L. E. Bové, R. Gaal, Z. Raza, A.-A. Ludl, S. Klotz, A. M. Saitta, A. F. Goncharov, P. Gillet, Effect of salt on the H-bond symmetrization in ice. *Proc. Natl. Acad. Sci. U.S.A.* **112**, 8216–8220 (2015). doi:10.1073/pnas.1502438112 Medline

29. C. Herzberg, K. Condie, J. Korenaga, Thermal history of the Earth and its petrological expression. *Earth Planet. Sci. Lett.* **292**, 79–88 (2010). doi:10.1016/j.epsl.2010.01.022

30. C. T. A. Lee, P. Luffi, T. Plank, H. Dalton, W. P. Leeman, Constraints on the depths and temperatures of basaltic magma generation on Earth and other terrestrial planets using new thermobarometers for mafic magmas. *Earth Planet. Sci. Lett.* **279**, 20–33 (2009). doi:10.1016/j.epsl.2008.12.020

31. C. A. Dalton, C. H. Langmuir, A. Gale, Geophysical and geochemical evidence for deep temperature variations beneath mid-ocean ridges. *Science* **344**, 80–83 (2014). doi:10.1126/science.1249466 Medline

32. C. R. Bina, A. Navrotsky, Possible presence of high-pressure ice in cold subducting slabs. *Nature* **408**, 844–847 (2000). doi:10.1038/35048555 Medline

33. R. J. Angel, M. L. Mazzucchelli, M. Alvaro, P. Nimis, F. Nestola, Geobarometry from host-inclusion systems: The role of elastic relaxation. *Am. Mineral.* **99**, 2146–2149 (2014). doi:10.2138/am-2014-5047

34. V. B. Prakapenka, A. Kubo, A. Kuznetsov, A. Laskin, O. Shkurikhin, P. Dera, M. L. Rivers, S. R. Sutton, Advanced flat top laser heating system for high pressure research at GSECARS: Application to the melting behavior of germanium. *High Press. Res.* **28**, 225–235 (2008). doi:10.1080/08957950802050718

35. P. Dera, K. Zhuravlev, V. B. Prakapenka, M. L. Rivers, G. J. Finkelstein, O. Grubor-Urosevic, O. Tschauner, S. M. Clark, R. T. Downs, High pressure single-crystal micro X-ray diffraction analysis with GSE_ADA/RSV software. *High Press. Res.* **33**, 466–484 (2013). doi:10.1080/08957959.2013.806504

36. C. Prescher, V. B. Prakapenka, DIOPTAS: A program for reduction of two-dimensional X-ray diffraction data and data exploration. *High Press. Res.* **35**, 223–230 (2015). doi:10.1080/08957959.2015.1059835

37. W. Kraus, G. Nolze, PowderCell—a program for the representation and manipulation of crystal structures and calculation of the resulting X-ray powder patterns. *J. Appl. Crystallogr.* **29**, 301–303 (1996). doi:10.1107/S0021889895014920

38. S. Klotz, L. E. Bove, T. Strässle, T. C. Hansen, A. M. Saitta, The preparation and structure of salty ice VII under pressure. *Nat. Mater.* **8**, 405–409 (2009). doi:10.1038/nmat2422 Medline

39. W. F. Kuhs, J. L. Finney, C. Vettier, D. V. Bliss, Structure and hydrogen ordering in ices VI, VII, and VIII by neutron powder diffraction. *J. Chem. Phys.* **81**, 3612–3623 (1984). doi:10.1063/1.448109

40. H. Putz, J. C. Schön, M. Jansen, Combined method for *ab initio* structure solution from powder diffraction data. *J. Appl. Crystallogr.* **32**, 864–870 (1999). doi:10.1107/S0021889899006615

41. P. Dera, C. T. Prewitt, S. Japel, D. L. Bish, C. T. Johnston, Pressure-controlled polytypism in hydrous layered materials. *Am. Mineral.* **88**, 1428–1435 (2003). doi:10.2138/am-2003-1006

42. M. Guthrie, R. Boehler, C. A. Tulk, J. J. Molaison, A. M. dos Santos, K. Li, R. J. Hemley, Neutron diffraction observations of interstitial protons in dense ice. *Proc. Natl. Acad. Sci. U.S.A.* **110**, 10552–10556 (2013). doi:10.1073/pnas.1309277110 Medline

43. A.-A. Ludl, L. E. Bové, D. Corradini, A. M. Saitta, M. Salanne, C. L. Bull, S. Klotz, Probing ice VII crystallization from amorphous NaCl-D_2O solutions at gigapascal pressures. *Phys. Chem. Chem. Phys.* **19**, 1875–1883 (2017). doi:10.1039/C6CP07340A Medline

44. A. F. Goncharov, V. V. Struzhkin, M. S. Somayazulu, R. J. Hemley, H. K. Mao, Compression of ice to 210 gigapascals: Infrared evidence for a symmetric hydrogen-bonded phase. *Science* **273**, 218–220 (1996). doi:10.1126/science.273.5272.218 Medline

45. K. Aoki, H. Yamawaki, M. Sakashita, Observation of Fano interference in high-pressure ice VII. *Phys. Rev. Lett.* **76**, 784–786 (1996). doi:10.1103/PhysRevLett.76.784 Medline

46. D. L. Decker, High-pressure equation of state for NaCl, KCl, and CsCl. *J. Appl. Phys.* **42**, 3239–3244 (1971). doi:10.1063/1.1660714

47. E. J. Tronche, M. van Kan Parker, J. de Vries, Y. Wang, T. Sanehira, J. Li, B. Chen, L. Gao, S. Klemme, C. A. McCammon, W. van Westrenen, The thermal equation of state of $FeTiO_3$ ilmenite based on in situ X-ray diffraction at high pressures and temperatures. *Am. Mineral.* **95**, 1708–1716 (2010). doi:10.2138/am.2010.3410

48. S. Redfern, R. Angel, High-pressure behaviour and equation of state of calcite, $CaCO_3$. *Contrib. Mineral. Petrol.* **134**, 102–106 (1999). doi:10.1007/s004100050471

49. M. Merlini, F. Sapelli, P. Fumagalli, G. D. Gatta, P. Lotti, S. Tumiati, M. Abdellatief, A. Lausi, J. Plaisier, M. Hanfland, W. Crichton, J. Chantel, J. Guignard, C. Meneghini, A. Pavese, S. Poli, High-temperature and high-pressure behavior of carbonates in the ternary diagram $CaCO_3$-$MgCO_3$-$FeCO_3$. *Am. Mineral.* **101**, 1423–1430 (2016). doi:10.2138/am-2016-5458

50. W. D. Bischoff, F. C. Bishop, F. T. Mackenzie, Biogenically produced magnesian calcite: Inhomogeneities in chemical and physical properties; comparison with synthetic phases. *Am. Mineral.* **68**, 1183–1188 (1983).

51. P. Gillet, G. Fiquet, I. Daniel, B. Reynard, M. Hanfland, Equations of state of C-12 and C-13 diamond. *Phys. Rev. B* **60**, 14660–14664 (1999). doi:10.1103/PhysRevB.60.14660

52. R. J. Angel, M. Alvaro, F. Nestola, M. L. Mazzucchelli, Diamond thermoelastic properties and implications for determining the pressure of formation of diamond-inclusion systems. *Russ. Geol. Geophys.* **56**, 211–220 (2015). doi:10.1016/j.rgg.2015.01.014

53. H. J. McSkimin, W. L. Bond, Elastic moduli of diamond. *Phys. Rev.* **105**, 116–121 (1957). doi:10.1103/PhysRev.105.116

54. J. Thewlis, A. R. Davey, Thermal expansion of diamond. *Philos. Mag.* **1**, 409–414 (1956). doi:10.1080/14786435608238119

55. J. F. Lin, E. Gregoryanz, V. V. Struzhkin, M. Somayazulu, H. K. Mao, R. J. Hemley, Melting behavior of H_2O at high pressures and temperatures. *Geophys. Res. Lett.* **32**, L11306 (2005). doi:10.1029/2005GL022499

56. F. Datchi, P. Loubeyre, R. LeToullec, Extended and accurate determination of the melting curves of argon, helium, ice (H_2O), and hydrogen (H_2). *Phys. Rev. B* **61**, 6535 (2000). doi:10.1103/PhysRevB.61.6535

57. M. Ahart, K. A. Karandikar, S. Gramsch, R. Boehler, R. J. Hemley, High P-T Brillouin scattering study of H_2O melting to 26 GPa. *High Press. Res.* **34**, 327–336 (2014). doi:10.1080/08957959.2014.946504

58. E. H. Abramson, J. M. Brown, Equation of state of water based on speeds of sound measured in the diamond-anvil cell. *Geochim. Cosmochim. Acta* **68**, 1827–1835 (2004). doi:10.1016/j.gca.2003.10.020

59. C. Sanchez-Valle, D. Mantegazzi, J. D. Bass, E. Reusser, Equation of state, refractive index and polarizability of compressed water to 7 GPa and 673 K. *J. Chem. Phys.* **138**, 054505 (2013). doi:10.1063/1.4789359 Medline